Accepted Manuscript
Version of Record at: https://doi.org/10.1021/acs.biomac.3c00418

# Sequence-encoded Differences in Phase Separation Enable Formation of Resilin-like Polypeptide-based Microstructured Hydrogels

*Sai S. Patkar,[1*] Cristobal Garcia Garcia,[1] Luisa L. Palmese,[1] Kristi L. Kiick[1,2,*]*

1. Department of Materials Science and Engineering, University of Delaware, Newark, Delaware 19716, United States

2. Department of Biomedical Engineering, University of Delaware, Newark, Delaware 19713, United States

* Corresponding Authors

KEYWORDS

Resilin-Like Polypeptides, Phase Transitions, Hydrogels, UCST

ABSTRACT

Microstructured hydrogels are promising platforms to mimic structural and compositional heterogeneities of native extracellular matrix (ECM). Current state-of-the-art soft matter patterning techniques for generating ECM mimics can be limited owing to their reliance on specialized equipment and multiple time- and energy-intensive steps. Here, a photocrosslinking methodology

that traps various morphologies of phase-separated multicomponent formulations of compositionally distinct resilin-like polypeptides (RLPs) is reported. Turbidimetry and quantitative $^{1}$H NMR spectroscopy were utilized to investigate the sequence-dependent liquid-liquid phase separation (LLPS) of multicomponent solutions of RLPs. Differences between the intermolecular interactions of two different photocrosslinkable RLPs and a phase-separating templating RLP were exploited for producing microstructured hydrogels with tunable control over pore diameters (ranging from 1.5 $\mu$m –150 $\mu$m) and shear storage moduli (ranging from 0.2kPa – 5 kPa). Culture of human mesenchymal stem cells demonstrated high viability and attachment on microstructured hydrogels, suggesting their potential for developing customizable platforms for regenerative medicine applications.

## 1. Introduction

The native extracellular matrix (ECM) is a three-dimensional (3D) network comprising proteins, proteoglycans, and glycoproteins which provides structural support to cells along with sophisticated and dynamic regulatory cues to facilitate cellular processes such as adhesion, migration, proliferation, differentiation, and survival.[1] Development of synthetic mimics of the native ECM has been enabled by hydrogels which are hydrophilic, water-swollen, and crosslinked polymeric networks.[2–4] The design of such highly tunable and modular synthetic matrices is a critical consideration when developing model 3D cell culture systems that can mimic structural and functional features of various organs.[5] Cell and organoid culture platforms could benefit significantly from materials that present spatially distinct biochemical and mechanobiological cues to regulate cell behavior and yield models of human disease or regenerative therapies.[6,7] Heterogenous hydrogel scaffolds, which can mimic features of the complex and dynamic nature

of the ECM, have been particularly useful for directing cell-matrix interactions in 3D cultures, and have been utilized to guide 3D cell attachment, growth, and patterning.[8–10] Furthermore, differences in substrate curvature can influence the morphology of cellular attachment impacting their migration, differentiation, and spatiotemporal organization.[11–13] Hence, there are significant advantages in advancing methods for producing hydrogels with controlled microarchitectures characterized by distinct chemical, functional, and morphological domains.[14]

A facile one-step method for fabrication of microstructured hydrogels relies on capturing the phase separation morphology of multicomponent solutions undergoing liquid-liquid phase separation (LLPS).[15–17] The mechanism of phase separation and the resulting morphologies can be modulated via parameters such as temperature, pH, molecular weight, concentration, or macromolecular crowding agents including polyethylene glycol (PEG).[18–20] Nucleation and growth of spherical domains can be arrested, or percolated bicontinuous structures can be obtained via spinodal decomposition. Such microstructured hydrogels with interconnected pores (on the order of tens to hundreds of microns) have demonstrated improved cellular infiltration and proliferation, and they can also be exploited effectively for directing cell growth and organization.[21–26] However, due to its inherent thermodynamic instability, it is challenging to arrest spinodal decomposition, and percolating structures can rapidly morph into isolated spherical domains due to percolation-to-cluster transitions.[18,27,28] Compared to surfactants, colloidal particles offer a cell-friendly option to kinetically arrest spinodal decomposition and yield fully interconnected bicontinuous interfacially jammed emulsion gels (bijels).[25,26,29]

Other soft matter pattering techniques such as salt/porogen templating, gas foaming, cryogelation, microfluidics, lithography, photopatterning, electrospinning, and 3D printing have also been used to generate microstructured hydrogels.[18,30] However, the availability of specialized equipment, fabrication time, and cost must be evaluated for successful translational outcomes. Owing to its accessibility, salt/porogen templating is one of the most widely implemented techniques. Irregularly sized salt crystals of sodium chloride and calcium carbonate,[31] or degradable polymeric microparticles with defined sizes and geometries, have been used as templating agents.[32] Despite the simplicity of these methods, complete removal of salt templates is imperative to maintain osmolarity consistent with physiological conditions.[30] In addition to ensuring the cytocompatibility of the polymeric porogens, their degradation kinetics and degree of removal need to be consistent across samples to ensure high-fidelity fabrication. Opportunities therefore remain to develop additional accessible methods to produce well-defined, microstructured, and porous hydrogels.

Resilin-like polypeptides (RLPs) are recombinant intrinsically disordered protein polymers (IDPPs) that are derived from resilin, an elastomeric insect protein.[33,34] Owing to their outstanding mechanical properties, RLPs have emerged as popular candidates for developing regenerative therapies for mechanically active tissues.[33,35] Compared to reconstituted ECM materials (e.g., Matrigel, collagen), or synthetic polymers (e.g., polyethylene glycol), protein-engineered biopolymers such as RLPs present exceptional opportunities for independent tuning of storage moduli, degradation rates, and density of bioactive ligands.[5,36–38] Furthermore, altering key amino acid residues in the consensus sequence can trigger potent upper critical solution temperature (UCST) transitions.[39–41] This thermoresponsive LLPS of RLPs has been harnessed for generating

microstructured materials as cell-instructive matrices with locally heterogeneous micromechanical properties. Predominantly, the phase separation of multicomponent solutions of RLP and PEG has been arrested to yield hybrid hydrogels with tunable domain sizes and compositions.[19] Mannich-type reaction with small-molecule crosslinkers,[42] thiol-ene photocrosslinking for step-growth networks,[43] and radical chain-growth via photopolymerization of acrylate/acrylamide groups[44] have been used for successfully crosslinking solutions of RLP and PEG of complementary functionality prior to bulk phase separation. However, formulation of RLP/PEG solutions almost exclusively yields hydrogels with isolated RLP-rich domains in PEG-rich matrices of high bulk shear storage moduli ranging from 7.5kPa to 20 kPa.[17,44] Moreover, capturing complementary morphologies with PEG-rich domains interspersed in an RLP matrix is challenging due to the high concentration of the precursor formulations required and their rapid phase separation kinetics. We have thus sought opportunities for generating microstructured RLP matrices with tunable mechanical properties across a broader range of storage moduli useful for cell-based applications.

To overcome the challenges associated with traditional porogens, a positively charged and water soluble RLP was utilized in this study as a templating agent in multicomponent solutions with other photocrosslinkable RLPs. To alter the thermodynamics of phase separation, precise control over amino acid composition of the various RLPs was exploited to modulate their intermolecular and intramolecular interactions. Their thermally triggered phase separation was used to generate RLP hydrogels; after photocrosslinking, the sacrificial templating RLP could be easily removed by incubation in a buffer reservoir. Turbidimetry measurements of the different RLPs used in this system and their multicomponent solutions were performed to determine their thermoresponsive phase behavior. Quantitative $^{1}$H NMR spectroscopy of bulk phase-separated solutions provided

Accepted Manuscript
Version of Record at: https://doi.org/10.1021/acs.biomac.3c00418

insight into the differences in their phase separation and allowed for selection of candidates for formulating multicomponent precursor solutions that could be rapidly photocrosslinked to produce microstructured hydrogels. Confocal microscopy was utilized to investigate the resulting microstructures, and oscillatory shear rheology was used to evaluate the effect of generating pores of different sizes on the bulk mechanical properties of the microstructured hydrogels. Finally, their compatibility for culturing human mesenchymal stem cells (hMSCs) was assessed via Live/Dead viability assays.

## 2. Materials and Methods

### 2.1. Materials

The plasmid DNA encoding different RLPs (between BamHI and HindIII in pQE-80L) was purchased from Genscript Corporation (Piscataway, NJ). See Figure S1 for detailed sequence. Chemically competent cells of E. coli strain M15 [pREP4] were purchased from Qiagen (Valencia, CA) for transformation of recombinant plasmids. Isopropyl β-D-1-thiogalactopyranoside (IPTG) for induction of protein expression was purchased from Gold Bio (St. Louis, MO). RNase A for protein purification was purchased from Qiagen (Germantown, MD). MSP 96 target ground steel BC plate and Protein Standard II for MALDI-TOF MS were purchased from Bruker (Billerica, MA). Deuterated NMR solvents were purchased from Cambridge Isotope Laboratories (Tewksbury, MA). 0.5 mm thick silicone sheets and 5mm disposable biopsy punches were purchased from McMaster-Carr (Elmhurst, IL) and Integra Miltex (Mansfield, MA) respectively for creating hydrogel fabrication molds. Water for buffers or media was deionized and filtered

Accepted Manuscript
Version of Record at: https://doi.org/10.1021/acs.biomac.3c00418

using either a ThermoFisher Barnstead NANOpure diamond water purifier or a Milli-Q Synergy water purification system. All other reagents were purchased and used as received from Sigma-Aldrich (St. Louis, MO) or Fisher Scientific (Hampton, NH) unless indicated otherwise.

### 2.2. Protein expression and Purification

RLP-X sequences (based on the repeat GGRPSDSXGAPGGGN, see Figure S2 for the detailed sequence) were produced recombinantly; protein expression and purification were performed as previously reported by our laboratories.[40,42,44] These protocols were developed based on the QIAexpress system (Qiagen, Valencia, CA);[45] details can be found in the Supporting Information (SI). The purity and molecular weight of the different RLP-X constructs were confirmed via sodium dodecyl sulfate polyacrylamide gel electrophoresis (SDS-PAGE) and corroborated via matrix-assisted laser desorption/ionization-time-of-flight mass spectrometry (MALDI-TOF-MS) (Bruker MicroFlex MALDI-TOF, Billerica, MA), and ultra-performance liquid chromatography (UPLC) and electrospray ionization mass spectrometry (ESI-MS) (Waters Xevo G2-S Q-TOF MS with Acquity UPLC, Milford, MA) (Figures S3, S4, S5).

### 2.3. Acrylamide Functionalization and Characterization

The RLP-X constructs were functionalized with acrylamide groups via modification of the regularly positioned lysine residues encoded in the polypeptide chain with NHS-activated acrylic acid (NHS-Ac) (see Figure 1a). First, RLP-X was dissolved in 1X phosphate-buffered saline (PBS) (pH 7.4) at 10 mg/mL via stirring for 15 min. Separately, NHS-Ac was dissolved in anhydrous

Accepted Manuscript
Version of Record at: https://doi.org/10.1021/acs.biomac.3c00418

dimethyl sulfoxide (DMSO) to prepare a stock solution (50 mg/mL) which was added drop-wise addition to the RLP-X solution. The stoichiometric ratio of NHS-Ac to lysine was maintained at 0.5:1 to install 4 acrylamide groups per RLP-X molecule; the reaction was stirred for 4h at room temperature. To prevent precipitation during purification and to remove DMSO and byproducts, the reaction solution was diluted 8 times with DI water and transferred to 3.5 kDa dialysis tubing (Snakeskin™, Thermo Scientific) for dialysis against DI water in the cold room (4°C) with at least two changes of water with a final change dialyzed overnight. The purified RLP-X-4Ac was sterile-filtered, lyophilized, and stored at –20°C. The functionality of the RLP-X-4Ac was quantified via $^1$H NMR spectroscopy (Figure S6). ≈ 2.5 mg RLP-X-4Ac was dissolved in 500 $\mu$L deuterium oxide ($D_2O$) and analyzed using an AVANCE NEO 400 MHz NMR spectrometer (Bruker, Billerica, MA).The integration of aromatic protons of one tryptophan residue in RLP-L ($^1$H NMR (400 MHz, $D_2O$, δ): 7.00 – 7.60 (m, 5H)), and twelve tyrosine residues in RLP-Y tyrosine ($^1$H NMR(400 MHz, $D_2O$, δ): 6.67 (d, 2H), 6.98 (d, 2H)), was compared to the integration of the vinylic protons of the acrylamide that resulted from the reaction of the acrylic acid and lysine amine groups ($^1$H NMR (400 MHz, $D_2O$, δ): 5.65 – 6.30 (d, 3H)).

### 2.4. Turbidimetry Assays

#### 2.4.1. Turbidimetry via UV-Vis Spectroscopy

RLP-X or RLP-X-4Ac (based on the repeat GGRPSDSXGAPGGGN in which X represents W, Y or L) was dissolved in 1X PBS at various concentrations. The phase separation of solutions of different RLP-X-4Ac constructs was characterized by temperature-dependent measurements of

Accepted Manuscript
Version of Record at: https://doi.org/10.1021/acs.biomac.3c00418

their optical density at 350 nm, via ultraviolet (UV)-visible (Vis) spectroscopy, in a 10 mm path length quartz cuvette. A Cary 60 UV-Vis spectrophotometer equipped with a thermoelectric temperature controller and a house air line (to constantly purge the cuvettes of any condensing water vapor) was used for turbidimetry measurements. Turbidity data were acquired while cooling from 50°C to 0°C at a rate of 1°C/min.

The baseline was normalized to 0, and the transition temperature was defined as the temperature at which $OD_{600}$ first increased above 10% of the maximum value (here 0.3 units above the baseline). Owing to the lag in the broad absorbance peak in the high concentration samples in the far UV range of the spectra, changes in OD at 600 nm were used to determine the transition temperatures instead of changes in OD at 350nm. The turbidity data were fit to the Hill equation using the sigmoidal Hill1 function in Origin in order to compare differences in phase separation of the samples, and the corresponding Hill slopes are provided Table S1. UV-Vis turbidimetry was also used to obtain select data points to create the temperature vs composition phase diagram of psRLP-W in PBS by sequentially diluting 20 wt% solutions to 0.8 wt%.

### 2.4.2. Turbidimetry via Visual Determination of Cloud Points

RLP formulations of 14 wt%, 20 wt%, 26 wt% (w/v) total polypeptide concentrations were prepared with various mass ratios (0:100, 20:80, 30:70, 40:60, 50:50, 60:40, 70:30, 80:20, 100:0) of phase-separating RLP (psRLP-W) and photocrosslinkable RLP (pcRLP-Ac; aliphatic RLP-L-4Ac or aromatic RLP-Y-4Ac). Solutions were prepared in 1X PBS in a 0.2 mL PCR microtube. Phase diagrams for the multicomponent formulations were generated via visual turbidimetry. Each

formulation was warmed up to 85°C in an Eppendorf Mastercycler 5333 (Hamburg, Germany), and evaluated visually to determine the cloud point upon cooling (in 5°C increments). Transition from a clear solution to a turbid solution with no passage of light was defined as the cloud point. Closer to the first appearance of slight cloudiness, the sample was cooled in 0.2°C steps for obtaining data with higher resolution. The warming and cooling cycles were repeated thrice for the same solution to confirm the cloud point.

### 2.5. Characterization of Equilibrium Concentrations

RLP-X and/or RLP-X-4Ac were dissolved in 1X PBS at various concentrations and their solutions allowed to phase separate overnight at 0°C. Additionally, solutions of psRLP-W were allowed to phase separate at 0°C, 4°C and 15°C in order to expand the co-existence curve to lower and higher concentrations than those measured via turbidimetry assays. To plot the co-existence curve of psRLP-W, the data acquired by UV-Vis spectroscopy and quantitative $^{1}$H NMR spectroscopy were fitted to an asymmetric double sigmoidal curve by using the "Asym2Sig" function in Origin graphing software. Samples of 10 $\mu$L and 2 $\mu$L were collected carefully from the top and bottom layers respectively to prevent mixing of the two liquids and were subsequently dissolved in 500 $\mu$L deuterium oxide ($D_2O$) that contained 0.01 mg/mL 4,4-dimethyl-4-silapentane-1-sulfonic acid (DSS) as an internal reference. The concentration of each component was calculated from the $^{1}$H NMR spectrum acquired (64 scans) with a Bruker AVANCE NEO 400 MHz NMR spectrometer (Bruker, Billerica, MA) under quantitative conditions (with 0.01 mg/mL DSS as an internal standard). $T_1$ relaxation times for all RLP-X or RLP-X-4Ac constructs were

less than 2 seconds. For quantitative NMR analysis, a 90-degree pulse was used with a relaxation delay of 15 seconds.

### 2.6. Hydrogel Formation

RLP-X and RLP-X-4Ac were dissolved in 1X PBS at various concentrations and mixed to formulate different hydrogel precursor solutions corresponding to various concentrations and mass ratios. A stock solution of the photoinitiator lithium phenyl-2,4,6-trimethylbenzoyl phosphinate (LAP) was prepared in PBS at a concentration of 13.4 mg/mL. A 5% volume of LAP solution was added to the hydrogel precursor solution to obtain a final LAP concentration of 2.2 mM. The solution was warmed up in an Eppendorf 5333 MasterCycler Thermal Cycler to 70°C for 1 min, cooled down in an ice bath for 1 min, and transferred to a precooled silicon chamber (5 mm diameter, 0.5 mm thickness) on a Teflon tape-covered glass slide on ice. This was then covered with another precooled Teflon tape covered-glass slide to ensure formation of a flat and cylindrical hydrogel disc. The sample was then allowed to incubate for 5 min on ice to allow maturation of the phase separation for a set period of time. After 5 minutes, the sample was irradiated with UV light (365 nm, 5 mW/cm$^2$) for 5 min with a collimated LED UV light source (Thorlabs (Newton, NJ), Olympus, 365 nm, 745 mW). The UV intensity was confirmed with a radiometer. After 5 minutes of UV irradiation, the hydrogels were transferred to a petri dish containing 3 mL PBS as a buffer sink to wash out any non-covalently bound sacrificial RLP from the hydrogel. Hydrogels were stored at 4°C overnight prior to analysis via confocal microscopy and oscillatory shear rheology.

Accepted Manuscript
Version of Record at: https://doi.org/10.1021/acs.biomac.3c00418

### 2.7. Confocal Microscopy for Characterization of Microstructure

Hydrogel microstructure was characterized with a Zeiss 780 multiphoton microscope (Carl Zeiss, Inc., Thornwood, NY). A Chameleon Vision II Multiphoton laser with a 755 nm wavelength was used to excite the autofluorescence of the RLP, and an NDD detection system was used to image the multiphoton fluorescence and acquire confocal Z-stack images. The relatively small sizes of the pores and their abundance in all planes of the Z-stack resulted in granular rendering of maximum intensity projections, which made it challenging to visualize pore boundaries clearly for quantification. Hence, representative planes from the center of respective Z-stacks were used for visualization and to quantify pore diameters using ImageJ.

### 2.8. Oscillatory Rheology

The oscillatory rheology experiments were conducted on a stress-controlled AR-G2 rheometer (TA instruments, New Castle, DE) using 8 mm diameter stainless steel parallel-plate geometry. Following fabrication, hydrogels were incubated in PBS overnight at 4°C and warmed to room temperature at least one hour prior to testing. The swollen hydrogels were mounted on the rheometer plates at room temperature (24°C), as maintained by a Peltier device during the measurement. The geometry was set at a gap at which the normal force equaled 0.05 N to prevent slippage. Shear storage moduli (G') were recorded via time sweep measurements at a fixed amplitude strain of 1% and fixed frequency of 1 Hz within the linear viscoelastic regime of the hydrogels. Experiments were repeated on three individually prepared, synthetic replicates for each precursor composition.

Accepted Manuscript
Version of Record at: https://doi.org/10.1021/acs.biomac.3c00418

### 2.9. In vitro cell culture

Human bone-marrow-derived mesenchymal stem cells (hMSCs) (Lonza, Walkersville, MD, passage 4-6) were subcultured at a seeding density of 5000-6000 cells/cm$^2$ in T-182 flasks (Corning, New York, NY) at 37 °C with 5% carbon dioxide ($CO_2$) in MSCBM™ mesenchymal stem cell basal medium (Lonza, MD). Cell culture medium was refreshed every 3 days. Upon reaching ca. 80% confluence, cells were detached with Accutase™, counted, centrifuged, and resuspended in MSCBM medium at a cell density of 2x10$^6$ cells/mL. In a biosafety cabinet, various microstructured RLP hydrogels were prepared by adding 8 $\mu$L of hydrogel precursors into each well of a chambered coverslip (uncoated, $\mu$-Slide 15 Well 3D, ibidi, WI) using identical protocols described in Section 2.6, with the exception that the hydrogels were washed one time with 40 $\mu$L PBS and incubated in 40 $\mu$L MSCBM overnight at 37°C (5% $CO_2$) (rather than incubated in a 3 mL buffer sink). The following day, incubation media was removed and replaced with a cell suspension to achieve a seeding density of 2x10$^6$ cells/mL on the hydrogel surface. hMSC viability after 24h and 48h was assessed by performing Live/Dead assays (Invitrogen™, Waltham, MA). The hydrogels were washed with Hank's Balanced Salt Solution (HBSS, with calcium and magnesium) and placed in HBSS containing 2x10$^{-3}$M Calcein AM and 4x10$^{-3}$M ethidium homodimer for 20 min at 37 °C, 5% $CO_2$. After one wash with HBSS, the cells in and on the hydrogels were imaged in HBSS while still alive. The cells in and on the hydrogels were then imaged via laser scanning confocal microscopy on a Zeiss LSM 880 microscope (Carl Zeiss, Inc., Thornwood, NY); $\lambda_{ex}$ of RLP and Hoechst (405 nm), $\lambda_{ex}/\lambda_{em}$ of calcein-AM (495/515 nm), $\lambda_{ex}/\lambda_{em}$

Accepted Manuscript
Version of Record at: https://doi.org/10.1021/acs.biomac.3c00418

of ethidium homodimer (528/617 nm). Since the cells migrated to different Z-planes in the hydrogel, maximum intensity projections of representative Z-stack images are reported.

### 2.10. Statistics

Data are expressed as the mean ± standard error of the mean, unless otherwise specified. Statistical comparisons between pore diameters were performed by one-way analysis of variance (ANOVA) with Tukey HSD post-hoc tests. A two-way ANOVA was used to analyze differences in shear storage moduli of non-microstructured control hydrogels or microstructured hydrogels of different weight percents. If the F-test revealed significant statistical differences at the 0.05 level, pairwise comparisons were made using Tukey HSD post-hoc. p-values less than 0.05 were considered statistically significant. Statistical analysis was performed using JMP Pro 17 (JMP Statistical Discovery LLC).

## 3. Results and Discussion

Accepted Manuscript
Version of Record at: https://doi.org/10.1021/acs.biomac.3c00418

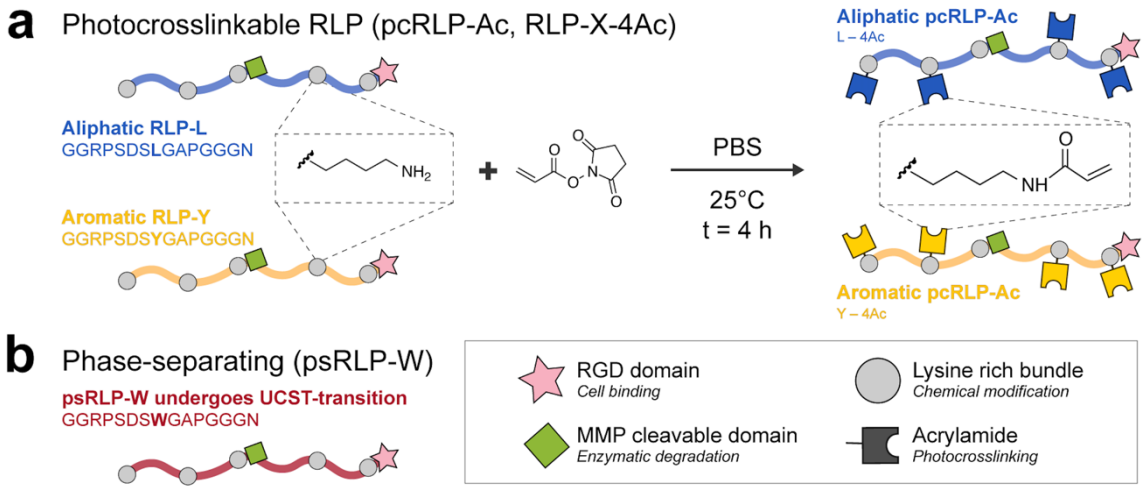


**Figure 1.** Schematic illustration of the different RLPs, their properties, and functionalization**.** a) Lysine residues in the aliphatic RLP-L and aromatic RLP-Y can be functionalized with photoreactive acrylamide groups via amide bond coupling to produce L-4Ac and Y-4Ac. b) Upon cooling below its UCST, psRLP-W phase separates and forms protein-rich coacervates.

### 3.1. Polypeptide Design, Synthesis and Characterization

The polypeptides reported in this study were derived from the consensus sequence of *Drosophila melanogaster* and synthesized in recombinant bacterial hosts based on previously reported protocols (Figures S1,S2).[40,42,44,46] Their successful production and purity were confirmed via MALDI-TOF-MS (Figure S3), analytical UPLC-ESI-MS (Figure S4), and SDS-PAGE (Figure S5). All RLPs reported in this study comprise a fibronectin-derived RGD domain for cell adhesion and a matrix metalloproteinase (MMP-1)[35,4717] cleavable domain to facilitate enzymatic degradation and matrix remodeling. An average of four photocrosslinkable groups were installed on each polypeptide chain to yield a pcRLP-Ac (RLP-X-4Ac) by reacting the primary amine

Accepted Manuscript
Version of Record at: https://doi.org/10.1021/acs.biomac.3c00418

groups of lysine with acrylic acid N-hydroxysuccinimide ester (Figure 1a). Two different RLPs, in which the central amino acids were substituted with leucine (RLP-L) or tyrosine (RLP-Y) residues, were employed to produce the aliphatic pcRLP-Ac (L-4Ac) and aromatic pcRLP-Ac (Y-4Ac) respectively (Figure 1a). $^{1}$H NMR spectroscopy was used to confirm the number of acrylamide groups installed (Figure S6). In a previous study, it was demonstrated that substitution of the central amino acid in the 12 repeats of GGRPSDSXGAPGGGN with select aromatic or aliphatic residues could be utilized for precisely tuning their LLPS.[40] RLP-W, RLP-Y, and RLP-F constructs in which the central amino acid was substituted with aromatic residues tryptophan, tyrosine, and phenylalanine respectively, underwent LLPS upon cooling, with RLP-W undergoing phase separation at transition temperatures 15 degrees higher than other aromatic analogues (RLP-Y or RLP-F).[40] For these reasons, RLP-W was employed as the phase-separating RLP (psRLP-W) for templating purposes (Figure 1b).

### 3.2. LLPS of psRLP-W/pcRLP-Ac Solutions

To screen favorable candidates for hydrogel formulation, turbidimetry measurements were performed to determine the UCST cloud points of the different RLP constructs and their mixed solutions at a final RLP concentration of 8 mg/mL in phosphate-buffered saline (Figure 2a). An increase in optical density at 600 nm upon cooling from 50°C was indicative of a temperature-triggered phase separation. At these relatively low concentrations, a UCST-like transition was observed only in psRLP-W, consistent with our previous investigations in which high concentrations of ammonium sulfate (a kosmotropic agent) and/or chemical modification with acrylamide groups were required to induce LLPS in the aromatically enriched sequences.[40] In this

Accepted Manuscript
Version of Record at: https://doi.org/10.1021/acs.biomac.3c00418

study, the propensity of psRLP-W to phase separate was exploited to trigger phase separation upon simple mixing with two different pcRLP-Ac constructs (Figure 2a). The differences (or lack thereof) between the slopes of the turbidimetry curves of psRLP-W and other psRLP-W/pcRLP-Ac solutions potentially indicated distinctions between their phase separation. Compared to the turbidity curve of solutions of psRLP-W alone, a 1:1 mixed solution of W and Y-4Ac had a slightly lower transition temperature, but a similar slope characteristic of rapid changes in turbidity with decreasing temperatures (Figure 2a, Tables 1, S1). The slopes of the turbidimetry curves of the aromatically enriched formulations resembled those reported previously for single component solutions of polypeptides undergoing UCST-type phase separation.[39,40,48] In contrast, a mixed solution of W and L-4Ac exhibited a higher transition temperature, but a slower, more gradual change in turbidity upon cooling.

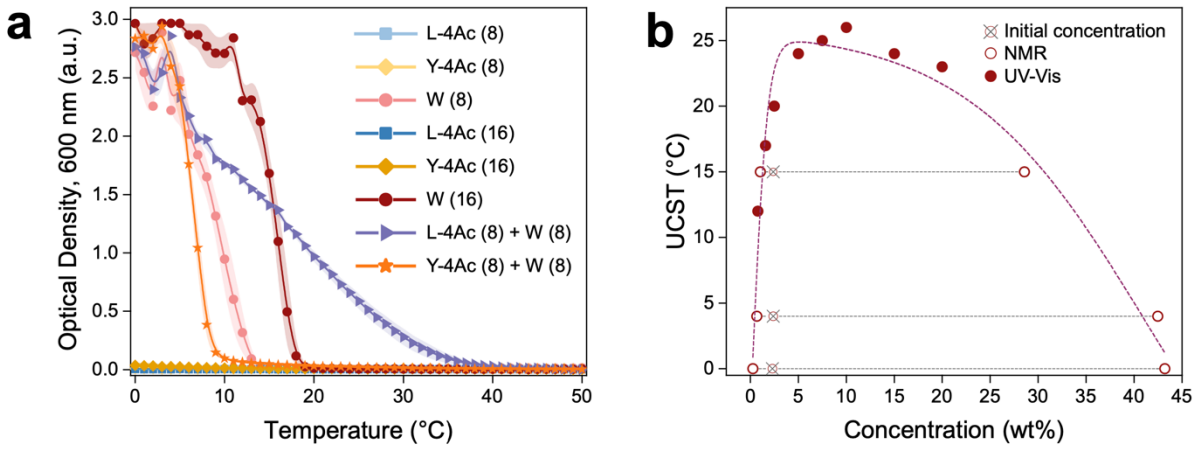


**Figure 2.** Phase separation of solutions of the different RLPs and their multicomponent formulations. a) UCST transition is observed only in psRLP-W constructs; psRLP-W promotes UCST transitions in 1:1 mixtures of psRLP-W and pcRLP-Ac solutions. Value in parenthesis represents polypeptide concentration in mg/mL. Turbidimetry assays were performed in phosphate-buffered saline, with cooling from 50°C to 0°C at a rate of 1°C/min. (n=3) b) Phase

Accepted Manuscript
Version of Record at: https://doi.org/10.1021/acs.biomac.3c00418

diagram of psRLP-W. Transition temperatures of psRLP-W are close to room temperature over a range of concentrations. Solid circles represent data acquired via UV-Vis turbidimetry. Open circles represent equilibrium concentrations of bulk phase separated emulsions acquired via quantitative $^{1}$H NMR spectroscopy. The co-existence curve of psRLP-W was generated by fitting the data to an asymmetric double sigmoidal curve ($R^2 = 0.96$).

**Table 1.** UCST values of psRLP-W solutions and psRLP-W/pcRLP-Ac (L-4Ac and Y-4Ac) solutions.

| Construct | UCST (°C) |
|---|---|
| L-4Ac (8 mg/mL, 16 mg/mL) | – |
| Y-4Ac (8 mg/mL, 16 mg/mL) | – |
| W (8 mg/mL) | 11.0 ± 0.6 |
| W (16 mg/mL) | 16.3 ± 0.3 |
| L-4Ac (8 mg/mL) + W (8 mg/mL) | 29.3 ± 1.5 |
| Y-4Ac (8 mg/mL) + W (8 mg/mL) | 7.3 ± 0.3 |

**Table 2.** Equilibrium concentrations of psRLP-W in PBS.

| Initial concentration (wt%) | Temperature (°C) | Top phase (wt%) | Bottom phase (wt%) |
|---|---|---|---|
| 2.4 | 15 | 1.1 | 28.6 |
| 2.4 | 4 | 0.7 | 42.5 |
| 2.3 | 0 | 0.3 | 43.2 |

Although this initial screening of trends in phase separation at low concentrations (0.8 wt% or 1.6 wt%) was informative, it was critical to evaluate the phase behavior of hydrogel precursor

formulations above the overlap polymer concentration (c*), to facilitate sufficient inter-chain crosslinking for the formation of robust networks. A phase diagram of temperature vs. composition was therefore generated to provide insight into the UCST phase behavior of the templating psRLP-W over a wide range of concentrations. A combination of UV-Vis turbidimetry and quantitative $^{1}$H NMR spectroscopy (Table 2) were employed to develop the coexistence curve in Figure 2b. For a wide range of concentrations, psRLP-W phase separated upon cooling below the transition temperatures which were close to room temperature. Subsequently, the phase separation of high concentration precursor formulations was characterized for determining the conditions for the production of microstructured hydrogels, and qualitative phase diagrams were generated via visual determination of cloud points (Figure 3). Visual turbidimetry permitted rapid assessment of cloud points while minimizing the quantity of RLP required for assessment. The visual cloud point values of 14 wt%, 20 wt% and 26 wt% psRLP-W were very close to the values obtained from UV-Vis turbidimetry and quantitative $^{1}$H NMR, thus confirming the utility of this approach.

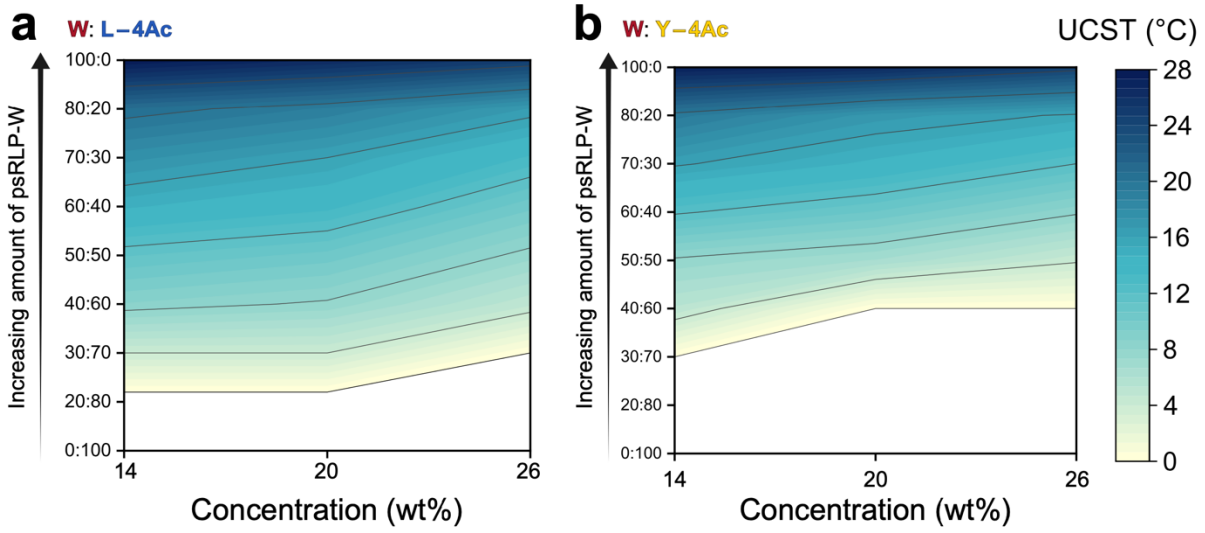

**Figure 3.** Phase diagrams of multicomponent formulations of psRLP-W and pcRLP-Ac. Contour plots displaying the relationship between the transition temperature and various combinations of distinct concentrations comprising increasing amounts of psRLP-W. White regions indicate that the system remained soluble for those compositions. a) Aliphatic pcRLP-Ac (L-4Ac). b) Aromatic pcRLP-Ac (Y-4Ac).

In the absence of psRLP-W in the formulation, neither aliphatic pcRLP-Ac (L-4Ac) nor aromatic pcRLP-Ac (Y-4Ac) solutions demonstrated any cloudiness at any of the concentrations or temperatures tested, indicative of the maintenance of a single phase. In both systems, the UCST of the mixed solutions increased with increasing amounts of psRLP-W in the formulation (Figure 3). Consistent with UV-Vis turbidimetry assays performed on low-concentration solutions, LLPS was induced at slightly higher transition temperatures in L-4Ac/W formulations compared to Y-4Ac/W formulations (Figures 2a, 3, Table 1). The transition temperatures of both L-4Ac/W and Y-4Ac/W formulations were below near or below room temperature for most compositions, making them comparable to the transition temperatures reported for other aqueous protein/polymer solutions, but dissimilar to the previously reported RLP/PEG formulations, which exhibited UCST values above room temperature.[42,49,50] Even at lower concentrations (4 wt%), the higher UCST values of RLP/PEG formulations with multiarm PEG were likely due to the reduction in the change of entropy of PEG arising from differences in architectural symmetry between the RLP and PEG components.[42,51]

Accepted Manuscript
Version of Record at: https://doi.org/10.1021/acs.biomac.3c00418

**Table 3.** Concentrations of pcRLP-Ac (L-4Ac or Y-4Ac) and psRLP-W in the top and bottom phases of phase separated multicomponent formulations of 14 wt%, 20 wt%, and 26 wt% (w/v) comprising 50/50 mass ratio.

| | RLP concentration (wt%, w/v) | | | | | | | | | | | |
|---|---|---|---|---|---|---|---|---|---|---|---|---|
| | L-4Ac/W formulations | | | | | | Y-4Ac/W formulations | | | | | |
| | L-4Ac | W | L-4Ac | W | L-4Ac | W | Y-4Ac | W | Y-4Ac | W | Y-4Ac | W |
| Initial | 7.0 | 7.0 | 10.0 | 10.0 | 13.0 | 13.0 | 7.0 | 7.0 | 10.0 | 10.0 | 13.0 | 13.0 |
| Top | 6.9 | 1.2 | 9.9 | 1.8 | 13.4 | 4.8 | 1.2 | 1.3 | 2.2 | 1.5 | 8.0 | 7.7 |
| Bottom | 1.7 | 27.2 | 0.6 | 12.5 | 6.4 | 13.7 | 9.8 | 20.7 | 11.6 | 15.5 | 4.1 | 23.7 |

Multicomponent formulations of 14 wt%, 20 wt%, and 26 wt% (w/v) comprising equal parts of pcRLP-Ac (L-4Ac or Y-4Ac) and psRLP-W (50/50 mass ratio) in PBS remained miscible at room temperature. Although cooling to 0°C initiated phase separation in all formulations, after overnight incubation at 0°C, characterization of the composition of the top and bottom phases via quantitative $^{1}$H NMR indicated clear differences in their phase separation (Table 3, Figures S7, S8, S9). The LLPS observed in L-4Ac/W solutions was similar to the previously reported LLPS in RLP/PEG solutions, in which phase separation over time yielded a PEG-rich top layer and an RLP-rich bottom layer.[42,44] Comparably, in this report, solutions of L-4Ac and W phase separated over time to form a L-4Ac-rich top layer and a W-rich bottom layer (Figure S7a, Table 3). Compared to the initial composition of the formulation, the concentration of L-4Ac in the top phase remained largely unchanged while the concentration of W decreased. In contrast, the concentration of L-4Ac in the bottom phase decreased, accompanied by an increase in the concentration of W, indicating that solutions of L-4Ac and W phase separated from each other. This propensity of L-4Ac and W to phase separate from each other was also reflected in the higher transition

Accepted Manuscript
Version of Record at: https://doi.org/10.1021/acs.biomac.3c00418

temperatures (Figures 2a, 3a, Table 1) and dissimilarity of the slope of the L-4Ac/W formulation compared to the turbidimetry trace of W alone (Figure 2a). Interestingly, contrasting behavior was observed in formulations containing Y-4Ac and W in which both components phase separated together to form a protein-rich bottom phase separated from a solvent-rich top layer, likely due to favorable interactions between the aromatic amino acids Y and W (Figure S7b, Table 3). For the 14 wt% and 20 wt% 50/50 Y-4Ac/W solutions, after 1 day, the top layer showed substantial depletion of both RLPs down to concentrations between 1% and 2%. The concentration of both RLPs in the protein-rich bottom phase increased, with a more appreciable increment in the concentration of RLP W compared to Y-4Ac. These favorable intermolecular interactions between the aromatic residues of Y-4Ac and W resulted in more similar compositions and overall lower transition temperatures (Figure 3b, Table 1). Despite the initial appearance of turbidity within 5 minutes, the highest concentration formulation of 26 wt% 50/50 Y-4Ac/W did not evolve into two distinct phases after incubation at 0°C overnight. Nevertheless, samples were taken from the top and bottom of the tube for comparison with the other formulations (Figure S8a, Table 3). After 32 days, two distinct layers appeared; with slow depletion of protein from the top layer which contained 0.9 wt% Y-4Ac and 7.4 wt% W (Figure S8b). The bottom protein-rich phase contained 7.5 wt% Y-4Ac and 21.9 wt% W.

### 3.3. LLPS of psRLP-W/pcRLP-Ac Formulations for Fabrication of Microstructured Hydrogels

Previous reports from our laboratories have demonstrated the utility of arresting the LLPS of multicomponent solutions of RLP and a macromolecular crowding agent (PEG) to fabricate

Accepted Manuscript
Version of Record at: https://doi.org/10.1021/acs.biomac.3c00418

microstructured hydrogels.[16,44] RLP-rich domains of various diameters were obtained via kinetic capture of maturing domains of different dimensions by photocrosslinking. Microscale RLP-rich domains ranging from 10$\mu$m to 67$\mu$m in diameter dispersed in a PEG-rich matrix were obtained depending on the pre-incubation time of RLP/PEG solutions (e.g., 0 min or 10 min) prior to photocrosslinking.[44] However, it has been extremely challenging to capture complementary morphologies of PEG-rich domains dispersed in an RLP-rich continuous matrix because of the rapid bulk phase separation at the high concentrations of formulations required. Therefore, the objective of the studies reported here was to overcome these limitations and to develop a common fabrication protocol for formulating pore-containing RLP hydrogels comprising different microstructures. Instead of changing the incubation time prior to crosslinking, modifying the amino acid composition of two different photocrosslinkable RLPs (L-4Ac or Y-4Ac) and the differences in their intermolecular interactions with psRLP-W were used to control the pore diameter and mechanical properties of the resulting microstructured hydrogels (Figures 4,5).

Precursor formulations of 14 wt%, 20 wt% and 26 wt% (w/v) were prepared by mixing equal parts of hydrogel-forming pcRLP-Ac (L-4Ac or Y-4Ac) and psRLP-W (50/50 mass ratio). The multicomponent RLP solutions were cooled to 0°C and subsequently photocrosslinked under cytocompatible conditions to arrest the observed LLPS for producing microstructured hydrogels. In the presence of cytocompatible, type I photoinitiator LAP, fast photopolymerization methods were utilized to crosslink formulations containing functionalized pcRLP-Ac upon UV irradiation (365 nm, 5 mW/cm$^2$). The chain growth polymerization of acrylamide moieties in the pcRLP-Ac-rich regions resulted in the formation of stable hydrogel networks. RLP-L and RLP-Y lacking acrylamide functionalization were incorporated in the formulations as controls to assess the impact

of including non-phase separating sacrificial agents on network formation. Owing to its highly charged and hydrophilic nature and lack of photofunctionality, any non-crosslinked RLP was easily removed upon incubation in excess PBS (Figure S10). Phase separation of the precursor formulations was reversible upon heating above their UCST (here 20°C) (Figure S11). Hence, of importance to note, when photocrosslinking was performed above their UCST (20°C) both L-4Ac/W and Y-4Ac/W formulations yielded hydrogels lacking any microstructure (Figure S12).

### 3.4. W-rich Coacervates Act As Templating Solutions for Fabrication of Microstructured hydrogels in L-4Ac/W Formulations

Formulations in which the constituent RLPs L-4Ac and W phase separated from each other resulted in microstructured hydrogels with decreasing pore diameters and increasing shear storage moduli as the weight percent of the precursor solutions increased (Figure 4). The morphology of this phase-separated system was arrested via photocrosslinking to yield crosslinked L-4Ac matrices comprising non-crosslinked psRLP-W-rich templating solutions (Figure 4a). Multiphoton microscopy was employed to distinguish between the microstructures obtained by varying the composition of the multicomponent formulation. The autofluorescence of crosslinked RLPs upon excitation with a 755 nm laser was used for visualization. Image analysis of representative Z stacks of microstructured hydrogels revealed that significantly decreasing pore diameters could be obtained by increasing the weight percent of the precursor solution. (Figure 4 b,c, 50/50 L-4Ac/W formulations, pore diameters of $15.4 \pm 0.6, 6.9 \pm 0.4, 5.2 \pm 0.2\ \mu$m for 14wt%, 20wt%, and 26 wt%). In the absence of psRLP-W in the formulation, control hydrogels lacking any microstructure were generated (Figure 4b, L-4Ac/L formulations).

Accepted Manuscript
Version of Record at: https://doi.org/10.1021/acs.biomac.3c00418

Once temperature-triggered phase separation is initiated, nuclei grow in size while the composition of each phase remains constant, with only the volume fraction of each phase changing until two distinct bulk phases are formed at equilibrium.[52–55] Thus, the final concentration of the crosslinked phase in the L-4Ac/W hydrogels is expected to match the composition of the top phase of the L-4Ac/W formulations in Table 3, indicating that microporous hydrogels of 6.9 wt%, 9.9 wt%, and 13.4 wt% are formed. Hydrogels with compositions closer to the overlap concentration (ca. 8.75 wt%)[46] were more sensitive to changes in concentration, resulting in hydrogels with more tunable shear storage moduli (Figure 4d). Oscillatory shear rheology data indicate that the shear storage moduli (G') of non-microstructured L-4Ac hydrogels significantly increased by an order of magnitude with increasing precursor concentrations (Figure 4d, 50/50 L-4Ac/L formulations, with G' values of 0.5 ± 0.0, and 2.9 ± 0.8 kPa for 20 wt% and 26 wt%). Although not statistically significant, similar trends were observed for the L-4Ac microstructured hydrogels (Figure 4d, 50/50 L-4Ac/W formulations, G' values of 0.2 ± 0.1, 0.8 ± 0.1, and 5.4 ± 0.3 kPa for 14wt%, 20wt%, and 26 wt%). Formulations in which the total mass of psRLP-W was kept constant showed matching trends (Figure S13).

Porous L-4Ac hydrogels had higher or comparable shear storage moduli compared to bulk hydrogels of the same L-4Ac concentration (Figure S14a), in contrast to systems employing conventional salt/polymeric porogen templating methods in which an increase in pore volume results in hydrogels with lower mechanical strength.[30,56] Furthermore, the presence of a phase-separating templating solution was required for effective interchain crosslinking and network formation in the 14wt% 50/50 L-4ac/W formulation for fabricating robust 7 wt% microporous

hydrogels. Bulk hydrogels of 7 wt% L-4Ac, or those prepared from a 14 wt% (50/50 L-4Ac/L) precursor comprising a non-phase separating templating solution, were too fragile for handling and characterization (Figures 4, S14a). This observed improvement in the mechanical properties of microstructured hydrogels (L-4Ac/W formulations) may be ascribed here to increased self-association and interactions among polypeptide chains upon phase separation (Figures S15, S16, S17) and is consistent with the improved toughness and viscoelasticity of hydrogels comprising phase-separated polymer domains.[57] Similar increase in G' was observed by Guo et al. below the UCST of dual thermoresponsive hybrid poly(N-acryloylglycinamide) and poly(N-isopropylacrylamide) hydrogels.[58]

Accepted Manuscript
Version of Record at: https://doi.org/10.1021/acs.biomac.3c00418

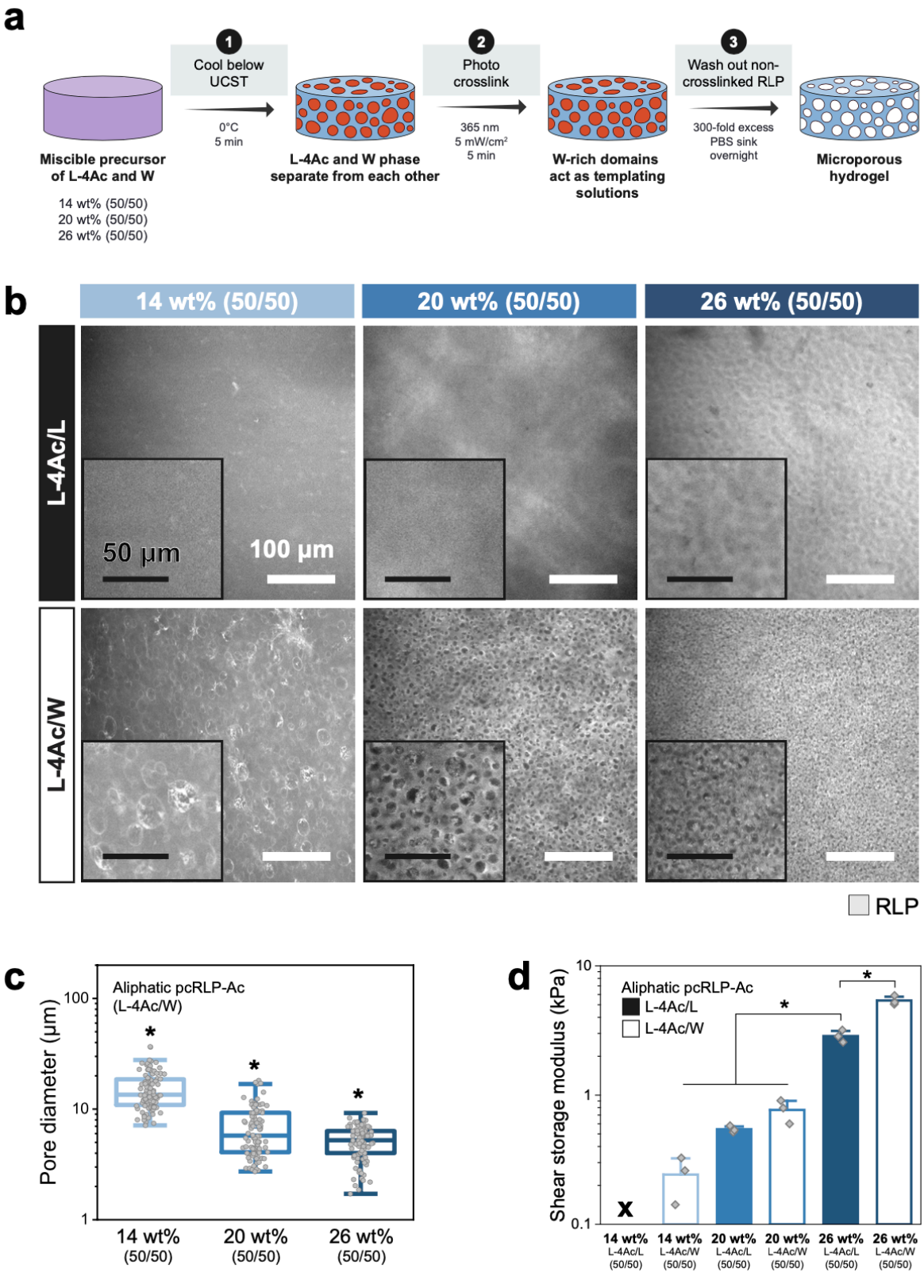

**Figure 4.** Microstructured hydrogels via phase separation of aliphatically enriched L-4Ac and the aromatic W formulations. a) Schematic illustration depicting the process for fabrication of microstructured hydrogels with tunable pore diameters and shear storage moduli. Cooling below the UCST causes L-4Ac and W to phase separate. W-rich coacervates act as microscale templating solutions during the photocrosslinking of the L-4Ac-rich complementary phase. Washing out any non-crosslinked RLP yields microporous hydrogels. b) Autofluorescence images of photocrosslinked RLP hydrogels. Maximum intensity projections of Z-stacks appeared grainy upon superimposition. Hence for clarity of visualization of pore boundaries, representative planes from the center of respective confocal Z-stacks are presented. The white signal corresponds to the autofluorescence of RLP. Insets represent expanded micrographs; Scale bars, 100 μm and 50 μm for the inset. c) Pore diameter significantly decreased with increasing weight percent. Box plot showing statistical distribution of the data for pore diameters obtained for each weight percent. * represents statistically significant differences between the mean pore diameters ($p < 0.05$ by ANOVA with Tukey HSD, n=100). d) Mechanical characterization of RLP hydrogels via oscillatory rheology demonstrated that shear storage moduli increased with increasing weight percent. x indicates that the hydrogel was too fragile for handling and characterization. * represents statistically significant differences between the mean shear storage moduli. ($p <0.05$ by two-way ANOVA with Tukey HSD, n=3)

### 3.5. Solvent-rich Domains Act As Templating Solutions for Fabrication of Microstructured Hydrogels in Y-4Ac/W Formulations

Formulations in which the constituent RLPs Y-4Ac and W phase separated together from the solvent resulted in microstructured hydrogels with different pore diameters but similar shear

Accepted Manuscript
Version of Record at: https://doi.org/10.1021/acs.biomac.3c00418

storage moduli even as the weight percent of the precursor solutions increased (Figure 5). The morphology of this phase-separated system was arrested via photocrosslinking to yield crosslinked Y-4Ac matrices that contained non-crosslinked solvent-rich templating solutions (Figure 5a). Image analysis of representative Z stacks revealed that microstructured hydrogels could be obtained for select Y-4Ac/W formulations. Beyond a certain required concentration in which no pores were observed (14 wt%), pore diameters significantly decreased with increasing concentrations (Figure 5b,c; 50/50 Y-4Ac/W formulations, pore diameters of 22.0 ± 1.8, 16.0 ± 0.5 $\mu$m for 20 wt% and 26 wt%).

In recent reports from our laboratories, Rekhi et al. showed that decreasing the aromatic character of similar resilin-derived model artificial intrinsically disordered proteins (A-IDPs) capable of undergoing UCST behavior, led to fewer interchain contacts in the protein condensates.[59] In the current studies, as indicated by their opacity, it is possible that a higher extent of interchain contacts and polymerization-induced phase separation (PIPS)[60,61] in bulk Y-4Ac hydrogels afforded them higher shear storage moduli compared to L-4Ac bulk hydrogels of the same composition (Figures S14, S15, S16). Compared to a non-phase separated hydrogel, local enrichment of polypeptide likely results in formation of bicontinuous macro networks comprising crosslinked bundles of polypeptide chains interconnected within a solvent-rich phase (**Figure S17**). The possible formation of this macro network and a higher extent of interchain contacts may lead to the increase in shear storage moduli reported in **Figure S14.** Furthermore, when W caused Y-4Ac to separate from the solvent, there was a local increase in the Y-4Ac concentration, above c*, in the protein-rich phase (Figure S16, Table 3). The resulting Y-4ac concentration in the protein-rich phase in the Y-4Ac/W formulations was higher than the L-4Ac concentration in its L-

4Ac-rich protein phase when the different systems phase separated (Table 3). This resulted in higher G' values overall (Figure 5d, 50/50 Y-4Ac/W formulations, G' values of 1.9 ± 0.4, 2.7 ± 0.4, and 4.3 ± 1.2 kPa for 14 wt%, 20 wt%, and 26 wt%). Interestingly, the moduli of the homogeneous (non-microstructured) control Y-4Ac hydrogels were statistically similar to the corresponding formulations which yielded microstructured hydrogels (Figure 5d, 50/50 Y-4Ac/Y formulations, G' values of 2.2 ± 0.4 and 2.9 ± 0.9 kPa for 20 wt% and 26 wt%). Furthermore, porous Y-4Ac hydrogels had statistically similar shear storage moduli compared to bulk hydrogels of the same Y-4Ac concentration (Figure S14b). The lack of statistical differences between the G' values of all the Y-4Ac hydrogels could be attributed to PIPS (Figures S16, S17) and the relative similarity of the total Y-4Ac concentration in the protein-rich phase, which was well above c* (Table 3, Figure S14b, Figure S16). Similar trends were observed in microstructured hydrogels via phase separation of Y-4Ac/W formulations in which the total mass of psRLP-W was kept constant (Figure S18).

Although this system has been optimized for fabricating thin hydrogels (~ 0.5 mm thickness) upon irradiation with UV light (365 nm, 5mW/cm$^2$ for 5 minutes in the presence of 2.2 mM LAP), Fairbanks et al. have provided that PEG-diacrylate hydrogels with thickness up to 1 cm can be photocured by decreasing photoinitiator concentration, lengthening exposure times, and/or increasing irradiation intensity.[62] If robust temperature control can be ensured throughout the thickness of the hydrogel mold during fabrication, it is expected that this approach could be extended to the fabrication of thicker hydrogels.

Accepted Manuscript
Version of Record at: https://doi.org/10.1021/acs.biomac.3c00418

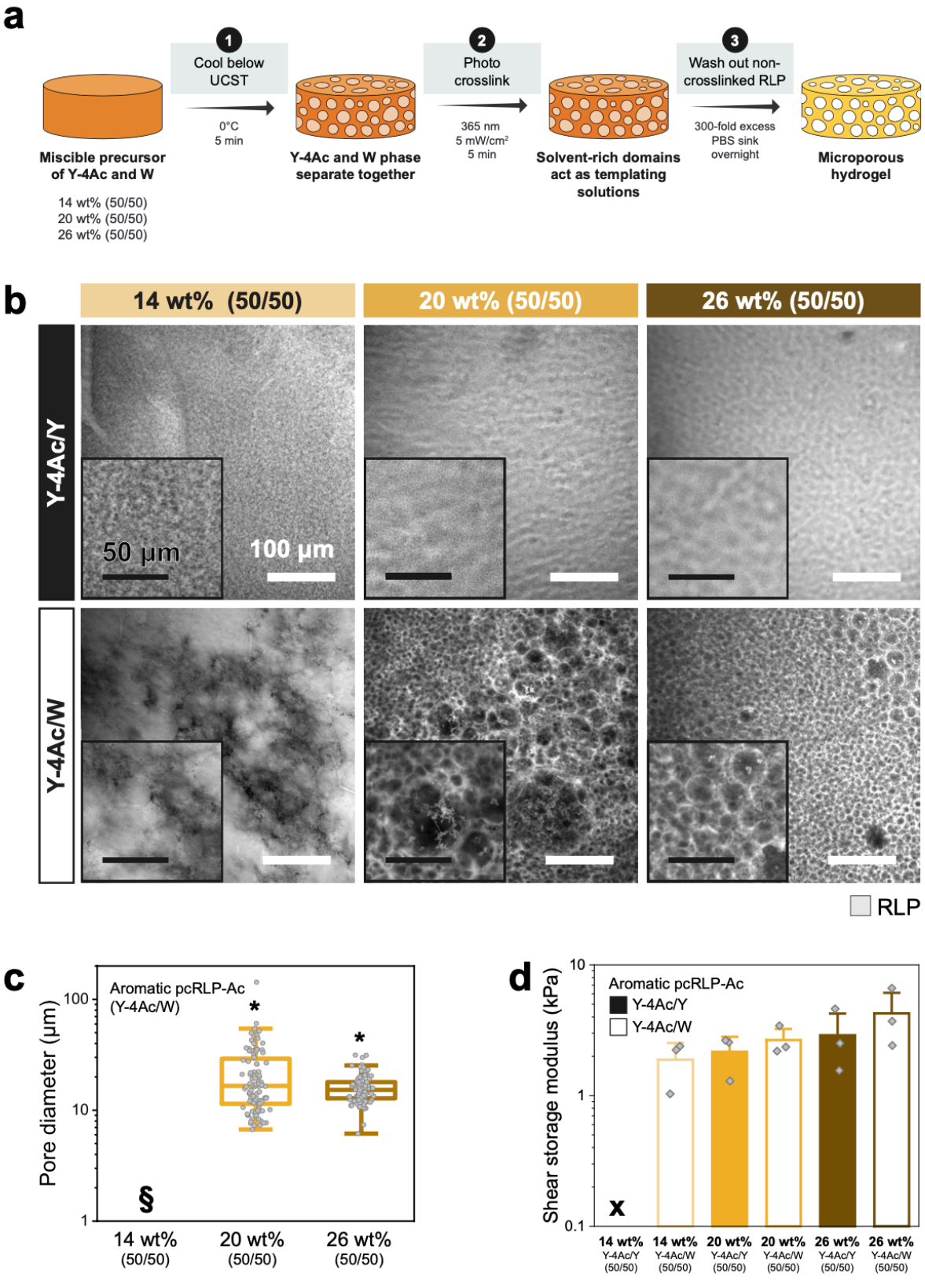

**Figure 5.** Microstructured hydrogels via phase separation of aromatically enriched Y-4Ac and W formulations. a) Schematic illustration depicting the process for fabricating microstructured hydrogels with constant shear storage moduli and tunable pore diameters. Upon cooling below the UCST, favorable interactions between Y-4Ac and W causes them to phase separate together from the solvent. Solvent-rich domains act as microscale templating solutions during the photocrosslinking of Y-4Ac in the Y-4ac and W-rich phase. Washing out any non-crosslinked RLP yields microporous hydrogels. b) Autofluorescence images of photocrosslinked RLP hydrogels. Maximum intensity projections of Z-stacks appeared grainy upon superimposition. Hence for clarity of visualization of pore boundaries, representative planes from the center of respective confocal Z-stacks are presented. The white signal corresponds to the autofluorescence of RLP. Insets represent expanded micrographs; Scale bars, 100 μm and 50 μm for the inset. c) Pore diameter significantly decreased with increasing weight percent. Box plot showing statistical distribution of the data for pore diameters obtained for each weight percent. § indicates absence of pores in the resulting morphology. * represents statistically significant differences between the mean pore diameters ($p < 0.05$ by ANOVA with Tukey HSD, n=100). d) Mechanical characterization of RLP hydrogels via oscillatory rheology demonstrated that RLP hydrogels were produced with no statistically significant differences between their mean shear storage moduli with increasing weight percent or introduction of microstructure ($p > 0.05$ by two-way ANOVA with Tukey HSD, n=3). x indicates that the hydrogel was too fragile for handling and characterization.

### 3.6. Cell Viability in Microstructured RLP Hydrogels

Accepted Manuscript
Version of Record at: https://doi.org/10.1021/acs.biomac.3c00418

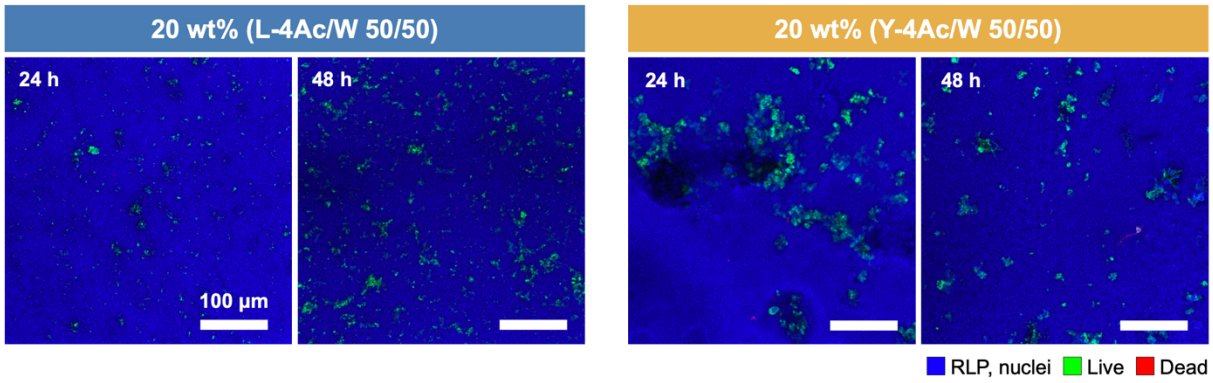


**Figure 6.** Microstructured RLP hydrogels are highly cytocompatible. Representative maximum intensity projection images from confocal Z-stacks for 2D culture of hMSCs in 20 wt% L-4Ac/W and 20 wt% Y-4Ac/W hydrogels at 24h and 48h. Colors indicate autofluorescence of RLP and nuclei (Hoechst, blue), live cells (calcein, green), and dead cells (ethidium homodimer, red). Scale bars, 100 µm.

The cytocompatibility and ability of microstructured RLP hydrogels to support the attachment of human mesenchymal stem cells (hMSCs) was evaluated by seeding cells on the surface of 20 wt% hydrogels (L-4Ac/W and Y-4Ac/W formulations) (Figure 6). Microstructured hydrogels with open and interconnected pore networks are desirable for promoting cell ingrowth, colonization, and vascularization.[24] However, confocal micrographs for both L-4Ac/W and Y-4Ac/W hydrogels likely suggest the presence of closed pores (**Figures 4b,5b**). Hence, MMP-1 cleavable GPQGIWGQG domains were incorporated in the middle of each RLP chain to allow for matrix remodeling in the presence of MMP-1 as previously reported.[35] Furthermore, all hydrogel formulations were equipped with RGD domains to promote integrin-mediated cell adhesion. As indicated by the representative confocal images, hMSCs remained highly viable after 48h; a

majority of the cells stained green representing metabolic activity. The mainly small and rounded morphology of the hMSCs was consistent with previous reports of 3D culture of hMSCs in RLP hydrogels.[44,63] After 48h, a small population of hMSCs also demonstrated elongated morphologies in the 20 wt% Y-4Ac/W hydrogels which had a wider distribution of pore diameters (almost an order of magnitude higher than the corresponding 20 wt% L-4Ac/W hydrogels (Figure S19)). Qualitative visual observations indicated that all hydrogels studied degraded over 48h in the presence of hMSCs, however no elongated morphologies were observed in non-microstructured RLP hydrogels (Figure S20). These observations are consistent with a similar study by Lee et al.,[64] in which an increasing amount of 10 kDa PEG-diol was employed as a polymeric porogen in fibrinogen-based hydrogels. Formulations comprising higher concentrations of the sacrificial PEG-diol increased the hydration and porosity while lowering the storage moduli of the resulting fibrinogen hydrogels. Smooth muscle cells (SMCs) adopted spindle-like morphologies more rapidly compared to the control hydrogels lacking the porosity afforded by a sacrificial porogen in which the encapsulated SMCs remained spherical.

Notably, an overall fewer number of cells and lower cell viability were observed on non-microstructured hydrogels fabricated from L-4Ac and L-4Ac/L formulations (Figure S20a, b). This is attributed to potential differences in their nanoporosity compared to hydrogels fabricated from Y-4Ac and Y-4Ac/Y formulations (Figures S15, S16). Similar trends were observed by Dong et al.;[65] in which PIPS was employed to generate nanoporous scaffolds with higher surface-to-volume ratios and improved permeability. Hep G2 epithelial cells demonstrated enhanced cell adhesion and viability on the nanoporous scaffolds compared to non-porous controls.[65] Similarly, in this study, the improved cell viability and adhesion on nanostructured (Y-4Ac, Y-4Ac/Y) and

Accepted Manuscript
Version of Record at: https://doi.org/10.1021/acs.biomac.3c00418

microstructured (L-4Ac/W, Y-4Ac/W) hydrogels might be a feature of altered cell anchorage owing to nanoscale topographical structures.[66–69]

The high cytocompatibility of these microstructured RLP hydrogels presents exciting opportunities for developing tunable platforms for the culture and spatial patterning of multiple cell types. Indeed, pore size is a key consideration when developing regenerative therapies[24] and the pore sizes of the hydrogel scaffolds reported in this study fit the requirements for various applications. For example, 5 $\mu$m pores are optimal for neovascularization,[70] 5-15 $\mu$m pores are preferable for fibroblast ingrowth,[71] and pores ranging from 20-125 $\mu$m have demonstrated success in regeneration of adult mammalian skin.[24,72,73] Importantly, the ability to specifically tune pore sizes without significantly altering shear storage moduli (Figure 5c,d) provides opportunities for developing highly modular and customizable cell-instructive platforms.

Efforts are underway to generate scaffolds with bicontinuous phases by arresting the phase separation of a multicomponent formulation undergoing spinodal decomposition. We intend to compare the scaffold colonization from the surface in systems with closed pores or bicontinuous microstructures. It should be noted that this approach for scaffold fabrication was unsuccessful for encapsulating hMSCs during hydrogel fabrication. Preliminary 3D cell encapsulation studies indicated that during the wash step to remove the templating psRLP-W phase, cells rapidly and preferentially migrated to the edges of the microchamber slide instead of attaching to the microstructured scaffold. Furthermore, it is likely that the presence of cells can alter the phase separation of the multicomponent formulation as a function of the cell concentration, shape, and

size. Hence, further optimization of these formulations in the presence of cells will be studied for their application in 3D cell encapsulation platforms.

## 4. Conclusions

In this study, the propensity of psRLP-W to undergo phase separation below its UCST was exploited to trigger LLPS in photocrosslinkable pcRLP-Ac at 0°C. The interactions between psRLP-W and pcRLP-Ac could be precisely controlled by selectively enriching pcRLP-Ac with aliphatic leucine residues or aromatic tyrosine residues. Photocrosslinking methods were utilized for the facile capture of sequence-dependent LLPS of multicomponent formulations of RLPs for fabricating microstructured hydrogels. $^{1}$H NMR spectroscopy and confocal microscopy data indicate that formulations in which the RLPs L-4Ac and psRLP-W preferred to phase separate from each other resulted in microporous hydrogels in which psRLP-W-rich domains acted as templating solutions. In contrast, formulations in which there were favorable intermolecular interactions between aromatic residues in Y-4Ac and psRLP-W resulted in phase separation of both proteins from the solvent and yielded solvent-rich domains as microscale templating agents during photocrosslinking. Furthermore, these materials were successfully employed for the culture of hMSCs without loss of viability. Hence, these microstructured hydrogels present exciting opportunities for developing highly customizable platforms for regenerative medicine applications.

ASSOCIATED CONTENT

**Supporting Information**. The following files are available free of charge (PDF).

Figures of RLP-X sequence, MALDI-TOF MS spectra, UPLC MS spectra, and SDS-PAGE of purified RLP-X constructs, $^{1}H$ NMR spectra of acrylamide functionalized RLPs, pictures of various multicomponent formulations undergoing phase separation over time, confocal micrographs of hydrogels fabricated above the UCST of the formulation (20°C), characterization of microstructured hydrogels formed via the phase separation of L-4Ac/W or Y-4Ac/W formulations with the total mass of W kept constant, comparison between the shear storage moduli of microporous hydrogels and bulk hydrogels of the same concentration, effect of fabrication temperature on the optical and mechanical properties of bulk hydrogels, schematic summarizing the differences between the L-4Ac/W and Y-4Ac/W systems, additional confocal micrographs comparing the cytocompatibility of non-microstructured RLP hydrogels.

## AUTHOR INFORMATION

### Corresponding Authors

* Kristi L. Kiick – Department of Materials Science and Engineering, Department of Biomedical Engineering, University of Delaware, Newark, Delaware, 19716, United States. Email: kiick@udel.edu

*Sai S. Patkar – Department of Materials Science and Engineering, University of Delaware, Newark, Delaware, 19716, United States. Email: spatkar@udel.edu

## ACKNOWLEDGMENTS

This research was primarily supported by National Science Foundation through the University of Delaware Materials Research Science and Engineering Center, DMR-2011824. Partial support for the work was also provided from NSF (from DMR-1609544; DMR- 2004796; DMR-0239744;

DMR-2004890); and the National Institutes of Health (P20 RR017716; RO1 DC011377). Microscopy equipment was acquired with shared instrumentation grants (S10 RR027273 and S10 OD016361) and access was supported by the NIH-NIGMS (P20 GM103446), the NIGMS (P20 GM139760), and the State of Delaware. The contents of this manuscript do not necessarily reflect the views of the funding agencies. The authors would also like to thank Dr. Shi (Steve) Bai of the Nuclear Magnetic Resonance (NMR) Laboratory at the University of Delaware for assisting with the $T_1$ relaxation time measurements.

REFERENCES

(1) Babu, S.; Albertino, F.; Omidinia Anarkoli, A.; De Laporte, L. Controlling Structure with Injectable Biomaterials to Better Mimic Tissue Heterogeneity and Anisotropy. *Adv. Healthcare Mater.* **2021**, *10* (11), 2002221. https://doi.org/10.1002/adhm.202002221.

(2) Lutolf, M. P.; Hubbell, J. A. Synthetic Biomaterials as Instructive Extracellular Microenvironments for Morphogenesis in Tissue Engineering. *Nat. Biotechnol.* **2005**, *23* (1), 47–55. https://doi.org/10.1038/nbt1055.

(3) Hoffman, A. S. Hydrogels for Biomedical Applications. *Adv. Drug Delivery Rev.* **2012**, *64* (Supplement), 18–23. https://doi.org/10.1016/j.addr.2012.09.010.

(4) Correa, S.; Grosskopf, A. K.; Lopez Hernandez, H.; Chan, D.; Yu, A. C.; Stapleton, L. M.; Appel, E. A. Translational Applications of Hydrogels. *Chem. Rev.* **2021**, *121* (18), 11385–11457. https://doi.org/10.1021/acs.chemrev.0c01177.

(5) Kratochvil, M. J.; Seymour, A. J.; Li, T. L.; Paşca, S. P.; Kuo, C. J.; Heilshorn, S. C. Engineered Materials for Organoid Systems. *Nat. Rev. Mater.* **2019**, *4* (9), 606–622.

https://doi.org/10.1038/s41578-019-0129-9.

(6) Blache, U.; Ford, E. M.; Ha, B.; Rijns, L.; Chaudhuri, O.; Dankers, P. Y. W.; Kloxin, A. M.; Snedeker, J. G.; Gentleman, E. Engineered Hydrogels for Mechanobiology. *Nat. Rev. Methods Primers* **2022**, *2* (1), 1–22. https://doi.org/10.1038/s43586-022-00179-7.

(7) Mirbagheri, M.; Adibnia, V.; Hughes, B. R.; Waldman, S. D.; Banquy, X.; Hwang, D. K. Advanced Cell Culture Platforms: A Growing Quest for Emulating Natural Tissues. *Mater. Horiz.* **2019**, *6* (1), 45–71. https://doi.org/10.1039/c8mh00803e.

(8) Neffe, A. T.; Pierce, B. F.; Tronci, G.; Ma, N.; Pittermann, E.; Gebauer, T.; Frank, O.; Schossig, M.; Xu, X.; Willie, B. M.; et al. One Step Creation of Multifunctional 3D Architectured Hydrogels Inducing Bone Regeneration. *Adv. Mater.* **2015**, *27* (10), 1738–1744. https://doi.org/10.1002/adma.201404787.

(9) Sun, J.; Wei, D.; Zhu, Y.; Zhong, M.; Zuo, Y.; Fan, H.; Zhang, X. A Spatial Patternable Macroporous Hydrogel with Cell-Affinity Domains to Enhance Cell Spreading and Differentiation. *Biomaterials* **2014**, *35* (17), 4759–4768. https://doi.org/10.1016/j.biomaterials.2014.02.041.

(10) Tang, S.; Richardson, B. M.; Anseth, K. S. Dynamic Covalent Hydrogels as Biomaterials to Mimic the Viscoelasticity of Soft Tissues. *Prog. Mater. Sci.* **2021**, *120*, 100738. https://doi.org/10.1016/j.pmatsci.2020.100738.

(11) Werner, M.; Blanquer, S. B. G.; Haimi, S. P.; Korus, G.; Dunlop, J. W. C.; Duda, G. N.; Grijpma, D. W.; Petersen, A. Surface Curvature Differentially Regulates Stem Cell Migration and Differentiation via Altered Attachment Morphology and Nuclear

Deformation. *Advanced Science* **2017**, *4* (2), 1600347. https://doi.org/10.1002/advs.201600347.

(12) Callens, S. J. P.; Uyttendaele, R. J. C.; Fratila-Apachitei, L. E.; Zadpoor, A. A. Substrate Curvature as a Cue to Guide Spatiotemporal Cell and Tissue Organization. *Biomaterials* **2020**, *232*, 119739. https://doi.org/10.1016/j.biomaterials.2019.119739.

(13) Pieuchot, L.; Marteau, J.; Guignandon, A.; Dos Santos, T.; Brigaud, I.; Chauvy, P. F.; Cloatre, T.; Ponche, A.; Petithory, T.; Rougerie, P.; et al. Curvotaxis Directs Cell Migration through Cell-Scale Curvature Landscapes. *Nat. Commun.* **2018**, *9* (1), 3995. https://doi.org/10.1038/s41467-018-06494-6.

(14) Kühn, S.; Sievers, J.; Stoppa, A.; Träber, N.; Zimmermann, R.; Welzel, P. B.; Werner, C. Cell-Instructive Multiphasic Gel-in-Gel Materials. *Adv. Funct. Mater.* **2020**, *30* (26), 1908857. https://doi.org/10.1002/adfm.201908857.

(15) Hori, A.; Watabe, Y.; Yamada, M.; Yajima, Y.; Utoh, R.; Seki, M. One-Step Formation of Microporous Hydrogel Sponges Encapsulating Living Cells by Utilizing Bicontinuous Dispersion of Aqueous Polymer Solutions. *ACS Appl. Bio Mater.* **2019**, *2* (5), 2237–2245. https://doi.org/10.1021/acsabm.9b00194.

(16) Lau, H. K.; Rattan, S.; Fu, H.; Garcia, C. G.; Barber, D. M.; Kiick, K. L.; Crosby, A. J. Micromechanical Properties of Microstructured Elastomeric Hydrogels. *Macromol. Biosci.* **2020**, *20* (5), 1900360. https://doi.org/10.1002/mabi.201900360.

(17) McGann, C. L.; Akins, R. E.; Kiick, K. L. Resilin-PEG Hybrid Hydrogels Yield Degradable Elastomeric Scaffolds with Heterogeneous Microstructure. *Biomacromolecules* **2016**, *17*

(1), 128–140. https://doi.org/10.1021/acs.biomac.5b01255.

(18) Garcia Garcia, C.; Kiick, K. L. Methods for Producing Microstructured Hydrogels for Targeted Applications in Biology. *Acta Biomater*. **2019**, *84*, 34–48. https://doi.org/10.1016/j.actbio.2018.11.028.

(19) Wang, B.; Patkar, S. S.; Kiick, K. L. Application of Thermoresponsive Intrinsically Disordered Protein Polymers in Nanostructured and Microstructured Materials. *Macromol. Biosci*. **2021**, *21* (9), 2100129.

(20) Lévesque, S. G.; Lim, R. M.; Shoichet, M. S. Macroporous Interconnected Dextran Scaffolds of Controlled Porosity for Tissue-Engineering Applications. *Biomaterials* **2005**, *26* (35), 7436–7446. https://doi.org/10.1016/j.biomaterials.2005.05.054.

(21) Peyton, S. R.; Kalcioglu, Z. I.; Cohen, J. C.; Runkle, A. P.; Van Vliet, K. J.; Lauffenburger, D. A.; Griffith, L. G. Marrow-Derived Stem Cell Motility in 3D Synthetic Scaffold Is Governed by Geometry along with Adhesivity and Stiffness. *Biotechnol. Bioeng*. **2011**, *108* (5), 1181–1193. https://doi.org/10.1002/bit.23027.

(22) Lien, S. M.; Ko, L. Y.; Huang, T. J. Effect of Pore Size on ECM Secretion and Cell Growth in Gelatin Scaffold for Articular Cartilage Tissue Engineering. *Acta Biomater*. **2009**, *5* (2), 670–679. https://doi.org/10.1016/j.actbio.2008.09.020.

(23) Griffon, D. J.; Sedighi, M. R.; Schaeffer, D. V.; Eurell, J. A.; Johnson, A. L. Chitosan Scaffolds: Interconnective Pore Size and Cartilage Engineering. *Acta Biomater*. **2006**, *2* (3), 313–320. https://doi.org/10.1016/j.actbio.2005.12.007.

(24) Annabi, N.; Nichol, J. W.; Zhong, X.; Ji, C.; Koshy, S.; Khademhosseini, A.; Dehghani, F.

Controlling the Porosity and Microarchitecture of Hydrogels for Tissue Engineering. *Tissue Eng., Part B* **2010**, *16* (4), 371–383. https://doi.org/10.1089/ten.teb.2009.0639.

(25) Thorson, T. J.; Botvinick, E. L.; Mohraz, A. Composite Bijel-Templated Hydrogels for Cell Delivery. *ACS Biomater. Sci. Eng.* **2018**, *4* (2), 587–594. https://doi.org/10.1021/acsbiomaterials.7b00809.

(26) Thorson, T. J.; Gurlin, R. E.; Botvinick, E. L.; Mohraz, A. Bijel-Templated Implantable Biomaterials for Enhancing Tissue Integration and Vascularization. *Acta Biomater.* **2019**, *94*, 173–182. https://doi.org/10.1016/j.actbio.2019.06.031.

(27) Läuger, J.; Lay, R.; Gronski, W. The Percolation-to-Cluster Transition during Spinodal Decomposition of an off-Critical Polymer Mixture. Observation by Light Scattering and Optical Microscopy. *J. Chem. Phys.* **1994**, *101* (8), 7181–7184. https://doi.org/10.1063/1.468304.

(28) Takeno, H.; Iwata, M.; Takenaka, M.; Hashimoto, T. Combined Light Scattering and Laser Scanning Confocal Microscopy Studies of a Polymer Mixture Involving a Percolation-to-Cluster Transition. *Macromolecules* **2000**, *33* (26), 9657–9665. https://doi.org/10.1021/ma001316u.

(29) Lee, M. N.; Mohraz, A. Bicontinuous Macroporous Materials from Bijel Templates. *Adv. Mater.* **2010**, *22* (43), 4836–4841. https://doi.org/10.1002/adma.201001696.

(30) De France, K. J.; Xu, F.; Hoare, T. Structured Macroporous Hydrogels: Progress, Challenges, and Opportunities. *Adv. Healthcare Mater.* **2018**, *7* (1), 1700927. https://doi.org/10.1002/adhm.201700927.

(31) Sergeeva, A.; Feoktistova, N.; Prokopovic, V.; Gorin, D.; Volodkin, D. Design of Porous Alginate Hydrogels by Sacrificial CaCO3 Templates: Pore Formation Mechanism. *Adv. Mater. Interfaces* **2015**, *2* (18), 1500386. https://doi.org/10.1002/admi.201500386.

(32) Huebsch, N.; Lippens, E.; Lee, K.; Mehta, M.; Koshy, S. T.; Darnell, M. C.; Desai, R. M.; Madl, C. M.; Xu, M.; Zhao, X.; et al. Matrix Elasticity of Void-Forming Hydrogels Controls Transplanted-Stem-Cell-Mediated Bone Formation. *Nat. Mater.* **2015**, *14* (12), 1269–1277. https://doi.org/10.1038/nmat4407.

(33) Balu, R.; Dutta, N. K.; Dutta, A. K.; Choudhury, N. R. Resilin-Mimetics as a Smart Biomaterial Platform for Biomedical Applications. *Nat. Commun.* **2021**, *12* (1), 149. https://doi.org/10.1038/s41467-020-20375-x.

(34) Patkar, S. S.; Garcia, C. G.; Kiick, K. L. Chapter 4. Intrinsically Disordered and Resilin-Based Protein Polymers for High-Performance Biomaterials Applications. *Biomimetic Protein Based Elastomers: Emerging Materials for the Future* **2022**, *10*, 73–107. https://doi.org/10.1039/9781788012720-00073.

(35) Li, L.; Mahara, A.; Tong, Z.; Levenson, E. A.; Mcgann, C. L.; Jia, X.; Yamaoka, T.; Kiick, K. L. Recombinant Resilin-Based Bioelastomers for Regenerative Medicine Applications. *Adv. Healthcare Mater.* **2016**, *5* (2), 266–275. https://doi.org/10.1002/adhm.201500411.

(36) Qian, Z. G.; Pan, F.; Xia, X. X. Synthetic Biology for Protein-Based Materials. *Curr. Opin. Biotechnol.* **2020**, *65*, 197–204. https://doi.org/10.1016/j.copbio.2020.04.004.

(37) Dimarco, R. L.; Heilshorn, S. C. Multifunctional Materials through Modular Protein Engineering. *Adv. Mater.* **2012**, *24* (29), 3923–3940.

https://doi.org/10.1002/adma.201200051.

(38) Garcia Garcia, C.; Patkar, S. S.; Wang, B.; Abouomar, R.; Kiick, K. L. Recombinant Protein-Based Injectable Materials for Biomedical Applications. *Adv. Drug Delivery Rev.* **2023**, *193*, 114673. https://doi.org/10.1016/j.addr.2022.114673.

(39) Dzuricky, M.; Rogers, B. A.; Shahid, A.; Cremer, P. S.; Chilkoti, A. De Novo Engineering of Intracellular Condensates Using Artificial Disordered Proteins. *Nat. Chem.* **2020**, *12* (9), 814–825. https://doi.org/10.1038/s41557-020-0511-7.

(40) Garcia Garcia, C.; Patkar, S. S.; Jovic, N.; Mittal, J.; Kiick, K. L. Alteration of Microstructure in Biopolymeric Hydrogels via Compositional Modification of Resilin-Like Polypeptides. *ACS Biomater. Sci. Eng.* **2021**, *7* (9), 4244–4257. https://doi.org/10.1021/acsbiomaterials.0c01543.

(41) Patkar, S. S.; Tang, Y.; Bisram, A. M.; Zhang, T.; Saven, J. G.; Pochan, D. J.; Kiick, K. L. Genetic Fusion of Thermoresponsive Polypeptides with UCST-Type Behavior Mediates 1D Assembly of Coiled-Coil Bundlemers. *Angew. Chem., Int. Ed.* **2023**, *62* (25), e202301331. https://doi.org/10.1002/anie.202301331.

(42) Lau, H. K.; Li, L.; Jurusik, A. K.; Sabanayagam, C. R.; Kiick, K. L. Aqueous Liquid–Liquid Phase Separation of Resilin-Like Polypeptide/Polyethylene Glycol Solutions for the Formation of Microstructured Hydrogels. *ACS Biomater. Sci. Eng.* **2016**, *3* (5), 757–766. https://doi.org/10.1021/acsbiomaterials.6b00076.

(43) McGann, C. L.; Dumm, R. E.; Jurusik, A. K.; Sidhu, I.; Kiick, K. L. Thiol-Ene Photocrosslinking of Cytocompatible Resilin-Like Polypeptide-PEG Hydrogels.

*Macromol. Biosci.* **2016**, *16* (1), 129–138. https://doi.org/10.1002/mabi.201500305.

(44) Lau, H. K.; Paul, A.; Sidhu, I.; Li, L.; Sabanayagam, C. R.; Parekh, S. H.; Kiick, K. L. Microstructured Elastomer-PEG Hydrogels via Kinetic Capture of Aqueous Liquid–Liquid Phase Separation. *Advanced Science* **2018**, *5* (6), 1–13. https://doi.org/10.1002/advs.201701010.

(45) Qiagen. *The QIAexpressionist – A Handbook for High-Level Expression and Purification of 6xHis-Tagged Proteins*, Fifth.; 2003.

(46) Rattan, S.; Li, L.; Lau, H. K.; Crosby, A. J.; Kiick, K. L. Micromechanical Characterization of Soft, Biopolymeric Hydrogels: Stiffness, Resilience, and Failure. *Soft Matter* **2018**, *14* (18), 3478–3489. https://doi.org/10.1039/c8sm00501j.

(47) Nagase, H.; Fields, G. B. Human Matrix Metalloproteinase Specificity Studies Using Collagen Sequence-Based Synthetic Peptides. *Biopolymers* **1996**, *40* (4), 399–416. https://doi.org/10.1002/(sici)1097-0282(1996)40:4<399::aid-bip5>3.0.co;2-r.

(48) Quiroz, F. G.; Chilkoti, A. Sequence Heuristics to Encode Phase Behaviour in Intrinsically Disordered Protein Polymers. *Nat. Mater.* **2015**, *14* (11), 1164–1171. https://doi.org/10.1038/nmat4418.

(49) Annunziata, O.; Asherie, N.; Lomakin, A.; Pande, J.; Ogun, O.; Benedek, G. B. Effect of Polyethylene Glycol on the Liquid-Liquid Phase Transition in Aqueous Protein Solutions. *Proc. Natl. Acad. Sci. U. S. A.* **2002**, *99* (22), 14165–14170. https://doi.org/10.1073/pnas.212507199.

(50) Annunziata, O.; Ogun, O.; Benedek, G. B. Observation of Liquid-Liquid Phase Separation

for Eye Lens S-Crystallin. *Proc. Natl. Acad. Sci. U. S. A.* **2003**, *100* (3), 970–974. https://doi.org/10.1073/pnas.242746499.

(51) Fredrickson, G. H.; Liu, A. J.; Bates, F. S. Entropic Corrections to the Flory-Huggins Theory of Polymer Blends: Architectural and Conformational Effects. *Macromolecules* **1994**, *27* (9), 2503–2511. https://doi.org/10.1021/ma00087a019.

(52) Alberti, S.; Gladfelter, A.; Mittag, T. Considerations and Challenges in Studying Liquid-Liquid Phase Separation and Biomolecular Condensates. *Cell* **2019**, *176* (3), 419–434. https://doi.org/10.1016/j.cell.2018.12.035.

(53) Tsai, F. J.; Torkelson, J. M. Roles of Phase Separation Mechanism and Coarsening in the Formation of Poly(Methyl Methacrylate) Asymmetric Membranes. *Macromolecules* **1990**, *23* (3), 775–784. https://doi.org/10.1021/ma00205a014.

(54) Tsai, F. J.; Torkelson, J. M. Microporous Poly(Methyl Methacrylate) Membranes: Effect of a Low-Viscosity Solvent on the Formation Mechanism. *Macromolecules* **1990**, *23* (23), 4983–4989. https://doi.org/10.1021/ma00225a018.

(55) Laxminarayan, A.; McGuire, K. S.; Kim, S. S.; Lloyd, D. R. Effect of Initial Composition, Phase Separation Temperature and Polymer Crystallization on the Formation of Microcellular Structures via Thermally Induced Phase Separation. *Polymer* **1994**, *35* (14), 3060–3068. https://doi.org/10.1016/0032-3861(94)90420-0.

(56) Stachowiak, A. N.; Bershteyn, A.; Tzatzalos, E.; Irvine, D. J. Bioactive Hydrogels with an Ordered Cellular Structure Combine Interconnected Macroporosity and Robust Mechanical Properties. *Adv. Mater.* **2005**, *17* (4), 399–403. https://doi.org/10.1002/ADMA.200400507.

(57) Sun, T. L.; Kurokawa, T.; Kuroda, S.; Ihsan, A. Bin; Akasaki, T.; Sato, K.; Haque, M. A.; Nakajima, T.; Gong, J. P. Physical Hydrogels Composed of Polyampholytes Demonstrate High Toughness and Viscoelasticity. *Nat. Mater.* **2013**, *12* (10), 932–937. https://doi.org/10.1038/nmat3713.

(58) Guo, H.; Mussault, C.; Marcellan, A.; Hourdet, D.; Sanson, N. Hydrogels with Dual Thermoresponsive Mechanical Performance. *Macromol. Rapid Commun.* **2017**, *38* (17), 1700287. https://doi.org/10.1002/marc.201700287.

(59) Rekhi, S.; Garcia Garcia, C.; Barai, M.; Rizuan, A.; Schuster, B. S.; Kiick, K. L.; Mittal, J. Expanding the Molecular Language of Protein Liquid-Liquid Phase Separation. 2023-03-03 *bioRxiv*, 2023.03.02.530853. https://doi.org/10.1101/2023.03.02.530853 (accessed 2023-07-01).

(60) Shibayama, M.; Morimoto, M.; Nomura, S. Phase Separation Induced Mechanical Transition of Poly(IV-Isopropylacrylamide)/Water Isochore Gels. *Macromolecules* **1994**, *27*, 5060–5066.

(61) Szczepanski, C. R.; Pfeifer, C. S.; Stansbury, J. W. A New Approach to Network Heterogeneity: Polymerization Induced Phase Separation in Photo-Initiated, Free-Radical Methacrylic Systems. *Polymer* **2012**, *53* (21), 4694–4701. https://doi.org/10.1016/j.polymer.2012.08.010.

(62) Fairbanks, B. D.; Schwartz, M. P.; Bowman, C. N.; Anseth, K. S. Photoinitiated Polymerization of PEG-Diacrylate with Lithium Phenyl-2,4,6-Trimethylbenzoylphosphinate: Polymerization Rate and Cytocompatibility. *Biomaterials* **2009**, *30* (35), 6702–6707. https://doi.org/10.1016/j.biomaterials.2009.08.055.

(63) Li, L.; Tong, Z.; Jia, X.; Kiick, K. L. Resilin-like Polypeptide Hydrogels Engineered for Versatile Biological Function. *Soft Matter* **2013**, *9* (3), 665–673. https://doi.org/10.1039/c2sm26812d.

(64) Lee, B. H.; Tin, S. P. H.; Chaw, S. Y.; Cao, Y.; Xia, Y.; Steele, T. W.; Seliktar, D.; Bianco-Peled, H.; Venkatraman, S. S. Influence of Soluble PEG-OH Incorporation in a 3D Cell-Laden PEG-Fibrinogen (PF) Hydrogel on Smooth Muscle Cell Morphology and Growth. *J. Biomater. Sci., Polym. Ed.* **2014**, *25* (4), 394–409. https://doi.org/10.1080/09205063.2013.862401.

(65) Dong, Z.; Cui, H.; Zhang, H.; Wang, F.; Zhan, X.; Mayer, F.; Nestler, B.; Wegener, M.; Levkin, P. A. 3D Printing of Inherently Nanoporous Polymers via Polymerization-Induced Phase Separation. *Nat. Commun.* **2021**, *12* (1), 1–12. https://doi.org/10.1038/s41467-020-20498-1.

(66) Guadarrama Bello, D.; Fouillen, A.; Badia, A.; Nanci, A. Nanoporosity Stimulates Cell Spreading and Focal Adhesion Formation in Cells with Mutated Paxillin. *ACS Appl. Mater. Interfaces* **2020**, *12* (13), 14924–14932. https://doi.org/10.1021/acsami.0c01172.

(67) Wang, T.; Feng, Z. Q.; Leach, M. K.; Wu, J.; Jiang, Q. Nanoporous Fibers of Type-I Collagen Coated Poly(L-Lactic Acid) for Enhancing Primary Hepatocyte Growth and Function. *J. Mater. Chem. B* **2013**, *1* (3), 339–346. https://doi.org/10.1039/c2tb00195k.

(68) Schulte, C.; Podestà, A.; Lenardi, C.; Tedeschi, G.; Milani, P. Quantitative Control of Protein and Cell Interaction with Nanostructured Surfaces by Cluster Assembling. *Acc. Chem. Res.* **2017**, *50* (2), 231–239. https://doi.org/10.1021/acs.accounts.6b00433.

(69) Huang, J.; Gräter, S. V; Corbellini, F.; Rinck, S.; Bock, E.; Kemkemer, R.; Kessler, H.; Ding, J.; Spatz, J. P. Impact of Order and Disorder in RGD Nanopatterns on Cell Adhesion. *Nano Lett.* **2009**, *9* (3), 1111–1116. https://doi.org/10.1021/nl803548b.

(70) Brauker, J. H.; Carr-Brendel, V. E.; Martinson, L. A.; Crudele, J.; Johnston, W. D.; Johnson, R. C. Neovascularization of Synthetic Membranes Directed by Membrane Microarchitecture. *J. Biomed. Mater. Res.* **1995**, *29* (12), 1517–1524. https://doi.org/10.1002/JBM.820291208.

(71) Klawitter, J. J.; Hulbert, S. F. Application of Porous Ceramics for the Attachment of Load Bearing Internal Orthopedic Applications. *J. Biomed. Mater. Res.* **1971**, *5* (6), 161–229. https://doi.org/10.1002/jbm.820050613.

(72) Yannas, I. V.; Lee, E.; Orgill, D. P.; Skrabut, E. M.; Murphy, G. F. Synthesis and Characterization of a Model Extracellular Matrix That Induces Partial Regeneration of Adult Mammalian Skin. *Proc. Natl. Acad. Sci. U. S. A.* **1989**, *86* (3), 933–937. https://doi.org/10.1073/pnas.86.3.933.

(73) Whang, K.; Elenz, D. R.; Nam, E. K.; Tsai, D. C.; Thomas, C. H.; Nuber, G. W.; Glorieux, F. H.; Travers, R.; Sprague, S. M.; Healy, K. E. Engineering Bone Regeneration with Bioabsorbable Scaffolds with Novel Microarchitecture. *Tissue Eng.* **1999**, *5* (1), 35–51. https://doi.org/10.1089/ten.1999.5.35.

Accepted Manuscript
Version of Record at: https://doi.org/10.1021/acs.biomac.3c00418

## For Table of Contents Use Only

Manuscript title: Sequence-encoded Differences in Phase Separation Enable Formation of Resilin-like Polypeptide-based Microstructured Hydrogels

*Author list: Sai S. Patkar, Cristobal Garcia Garcia, Luisa L. Palmese, Kristi L. Kiick*

## Table of Contents Graphic